APPLIED SCIENCES AND ENGINEERING

# Pulse-driven robot: Motion via solitary waves

**Bolei Deng[1], Liyuan Chen[1], Donglai Wei[2], Vincent Tournat[3], Katia Bertoldi[1,4]***

**The unique properties of nonlinear waves have been recently exploited to enable a wide range of applications, including impact mitigation, asymmetric transmission, switching, and focusing. Here, we demonstrate that the propagation of nonlinear waves can be as well harnessed to make flexible structures crawl. By combining experimental and theoretical methods, we show that such pulse-driven locomotion reaches a maximum efficiency when the initiated pulses are solitons and that our simple machine can move on a wide range of surfaces and even steer. Our study expands the range of possible applications of nonlinear waves and demonstrates that they offer a new platform to make flexible machines to move.**



## INTRODUCTION

Flexible structures capable of sustaining large deformations are attracting increasing interest not only for their intriguing static response (*1*–*3*) but also for their ability to support large amplitude elastic waves. It has been shown that by carefully controlling their geometry, the elastic energy landscape of these highly deformable systems can be engineered to enable the propagation of a variety of nonlinear waves, including vector solitons (*4*–*6*), transition waves (*7*–*9*), and rarefaction pulses (*10*, *11*). As such, the dynamic behavior of these structures not only displays a very rich physics but also offers new opportunities to manipulate the propagation of mechanical signals, enabling unidirectional propagation (*5*, *8*), mechanical logic (*7*), wave guiding (*12*, *13*), focusing (*14*), energy trapping (*15*), and mitigation (*10*) and damping of nonlinear periodic vibrations (*16*).

Here, inspired by both the retrograde peristaltic waves observed in earthworms (Fig. 1A) (*17*, *18*) and the ability of linear elastic waves to generate actuation in ultrasonic motors (*19*–*22*), we show that the propagation of nonlinear elastic waves in flexible structures provides opportunities for locomotion. To demonstrate the concept, we focus on a Slinky (Fig. 1B) (*23*–*26*)—an iconic stretchable toy that has captivated children and adults all over the world—and use it to realize a pulse-driven robot capable of propelling itself. Our simple machine is built by connecting the Slinky to a pneumatic actuator and using an electromagnet and a plate embedded between the loops to initiate nonlinear pulses that propagate from the front to the back. Notably, we find that the directionality of these pulses enables our simple robot to move forward. Moreover, our results indicate that the efficiency of such pulse-driven locomotion is optimal when the initiated waves are solitons—large amplitude (nonlinear) pulses with stable shape and constant velocity along propagation (*4*, *5*, *7*, *8*, *10*, *27*–*30*). As such, our study expands the range of possible applications of solitary waves and demonstrates that they can also be exploited as simple underlying engines to make flexible machines move.

## RESULTS

### Our Slinky-robot

We consider a metal Slinky with a length of 50 mm, an outer radius of 46.58 mm, and 90 loops, each with mass of $m$ = 1.01 g (Fig. 1B and section S1) and investigate how to exploit its intrinsic flexibility to realize a simple machine capable of rectilinear locomotion. To this end, we connect two Slinkies in series (for a total of 180 loops with length $L$ = 100 mm) and implement a simple actuation strategy based on a pneumatic actuator with a stroke of 140 mm (realized using a plastic syringe and a pump), an electromagnet (12V 20N, UXCELL), and three acrylic plates: a front plate inserted between the 20th and 21st loops of the Slinky, a loading plate with an embedded metallic nut fitted between the 30th and 31st loops, and a back plate used to support the tail (Fig. 1, C to E). To construct the robot, we take the pneumatic actuator, connect one of its ends to the front plate, and glue the electromagnet directly on the actuator (Fig. 1D and section S2). When the magnetic field is on, the loading plate remains in contact with the electromagnet, and the 10 loops of the Slinky between the front and loading plates can be stretched and shortened using the pneumatic actuator (Fig. 1E). We test the response of our simple machine by placing it on a smooth and flat surface (Canson Bristol paper) and repeatedly extending the 10 loops to $A_{in}$ ($A_{in}$ being the maximum distance between the loading and front plates; Fig. 2A). We monitor the tests with a high-speed camera (SONY RX100) and extract the displacement of the head, $u_h$, by tracking the position of the front plate via a superpixel-based method (*31*).

We start by actuating the Slinky while keeping the electromagnet on. In Fig. 2A, we report snapshots taken during a test, in which we repeatedly extend the front 10 loops to $A_{in}$ = 100 mm. Although the head of the robot reaches $u_h^{max} = \max(u_h) = 80$ mm when the actuator is fully extended, because of the symmetric frictional properties it goes back to the initial position at the end of each cycle (Fig. 2B); therefore, no forward motion is achieved (Fig. 2A and movie S1). Next, in an attempt to break symmetry and make our machine crawl, we turn off the magnetic field after stretching the front loops to $A_{in}$ = 100 mm. As soon as the electromagnet is turned off, the stretch in the front loops results in the excitation of a wave that propagates backward and reaches the back end of the Slinky (Fig. 2C and movie S1). Note that no reflected wave is observed in the Slinky because of the large energy dissipation upon collisions of the loops. We find that the propagation of this unidirectional pulse results in a nonzero $u_h$ at the end of each cycle—a clear indication that our robot moves forward. Specifically, if we denote with $u_h^{cycle}$ the difference between the displacement of the head at the end and at the beginning of a specific cycle, we find that $u_h^{cycle}/L = 0.32 \pm 0.02$ (green line in Fig. 2B). Therefore, our results indicate that the directionality introduced by the elastic waves can be exploited to make the robot move even in the presence of identical friction coefficients in backward

[1]Harvard John A. Paulson School of Engineering and Applied Sciences Harvard University, Cambridge, MA 02138, USA. [2]LAUM, CNRS, Le Mans Université, Av. O. Messiaen, 72085 Le Mans, France. [3]Kavli Institute, Harvard University, Cambridge, MA 02138, USA. [4]Wyss Institute for Biologically Inspired Engineering, Cambridge, MA 02138, USA. *Corresponding author. Email: bertoldi@seas.harvard.edu

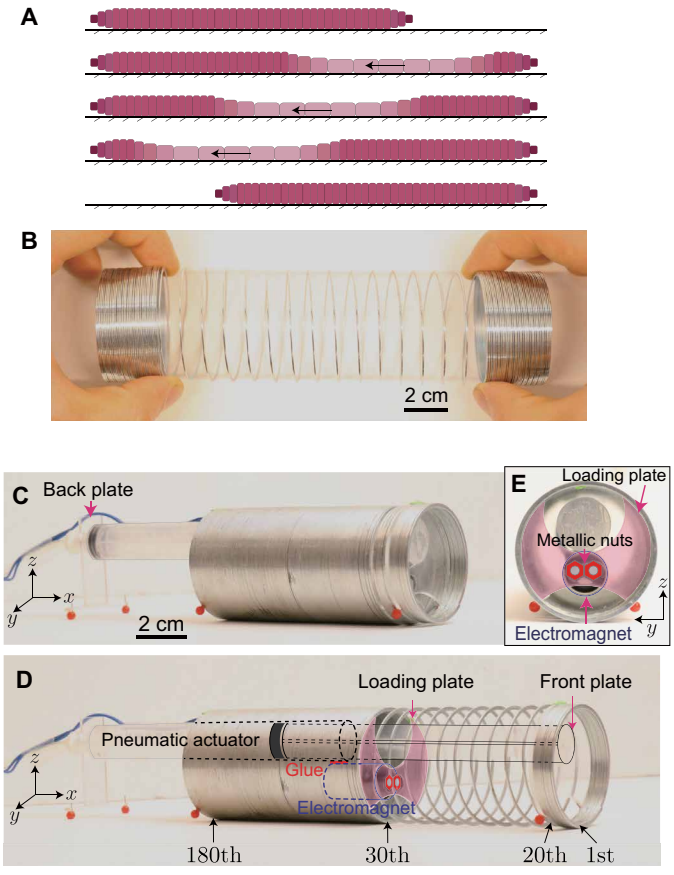


**Fig. 1. Our Slinky-robot.** (**A**) Schematic showing the locomotive mechanism of an earthworm based on retrograde peristaltic waves (i.e., waves that propagate in the opposite direction to locomotion). (**B**) Picture of metallic Slinky used in this study. (**C** and **D**) Pictures of our Slinky-robot (C) before and (D) after the pneumatic actuator is elongated. (**E**) Front view of the Slinky-robot showing the electromagnet. Note that several red plastic spheres are glued on to the Slinky to prevent it from rolling. Photo credit: Bolei Deng, Harvard University.

and forward directions. Furthermore, we also find that the phenomenon is robust as the robot behaves almost identically during various cycles (Fig. 2B).

Although our results indicate that the propagation of elastic pulses can be exploited to make our flexible machine crawl, they also reveal that the conditions used in our experiments are not optimal because there is noticeable backsliding immediately after the electromagnet is turned off. Specifically, if we focus on the first cycle, we find that $u_h$ suddenly drops from $u_h^{max} = 0.8L$ to about $u_h^{cycle} = 0.32L$ (Fig. 2B). To limit such backsliding, we increase the mass at the head, $m_h$. In Fig. 2D, we report the average value of $u_h^{cycle}$ over three cycles as a function of $m_h/m_{tot}$ ($m_{tot}$ being the total mass of the Slinky). While for the robot considered in Fig. 2C (for which $m_h/m_{tot} = 0.23$ ) $u_h^{cycle} = 0.32L$, we find that for $0.26 < m_h/m_{tot} < 0.39$ $u_h^{cycle}$ increases to $\sim 0.45L$. However, if $m_h/m_{tot} > 0.4$, $u_h^{cycle}$ then suddenly drops as the weight prevents the head to move forward when the pneumatic actuator is extended (movie S2).

Having identified an optimal range for $m_h$, we choose $m_h/m_{tot} = 0.32$ (resulting in $m_h = 78$ g and $m_{tot} = 246$ g) and investigate the effect of $A_{in}$ on the ability of our robot to crawl (Fig. 2E). As expected, we find that $u_h^{cycle}$ monotonically increases with $A_{in}$. However, more insight into the role of $A_{in}$ can be gained by calculating the efficiency η of such pulse-driven locomotion

$$\eta = \frac{W_{req}}{W_{in}} \tag{1}$$

where $W_{req}$ denotes the work required for the robot to move on the substrate against friction and $W_{in}$ is the work supplied to initiate the pulse. Specifically, if we denote with μ the friction coefficient between the Slinky and the substrate

$$W_{req} = \mu\, m_{tot} g\, u_h^{cycle} \tag{2}$$

and

$$W_{in} = \mu\, m_h g\, u_h^{max} + n_a \int_0^{\frac{A_{in}}{n_a}} F(\Delta u)\, d\Delta u \tag{3}$$

where $g$ is the gravitational constant, $n_a$ is the number of loops between the loading and front plates, and $F$ denotes the force required to stretch one loop of the Slinky by $\Delta u$. Note that the first term of Eq. 3 stands for the work done to move the head of the Slinky, while the second one represents the elastic energy stored in the front $n_a$ loops, which is eventually carried by the excited pulse. For the tests considered in Fig. 2, $n_a = 10$ and we measure $\mu = 0.17$. Moreover, we obtain the $F$-$\Delta u$ relation by conducting a quasistatic uniaxial tension test on a portion of the Slinky (see Fig. 2F and section S1 for details). In Fig. 2G, we plot the evolution of η as a function of $A_{in}$ obtained using Eqs. 1 to 3. Notably, we find that the efficiency of our machine is maximum for $A_{in} = 100$ mm. While in Fig. 2G we focus on a robot in which 10 loops are prestretched, this result persists also when we vary $n_a$. In particular, as shown in Fig. 2H, we find that for a wide range of $n_a$, the efficiency is maximum at $A_{in} = 100$ mm. However, such maximum decreases if $n_a < 7$ or $n_a > 16$. For large values of $n_a$, the energy carried by the excited pulses is small (see fig. S7) and not enough to make them propagate in the presence of friction (see movie S3). Differently, when $n_a$ is too small, the energy carried by the pulses is large, making the pulse to reach the back of the Slinky (see movie S3). At this point, $u_h^{cycle}$ saturates (see fig. S7) and the efficiency drops because part of the energy carried by the pulse is lost through collisions between the loops.

## Propagation of nonlinear waves

To understand why the efficiency of our robot is maximum for $A_{in} = 100$ mm, we carefully investigate the propagation of large-amplitude pulses through the Slinky. In these tests, we focus on a single Slinky (with $N = 90$ loops) and monitor the position of green markers located at every other loop. Moreover, to minimize the effect of friction, we lift the Slinky from the substrate and use a plastic rod to support it (Fig. 3A). As in the tests conducted on our Slinky-robot, we find that by prestretching 10 loops near the front and turning off the magnetic electromagnet, we can initiate elastic waves that propagate toward the back (Fig. 3B). Furthermore, these tests enable us to get deeper insights into the propagation of the pulses because we monitor the displacement of each individual loop (movie S4). In particular, two important features emerge from these tests. First, we find that the backward-propagating waves move the center of mass of the Slinky forward (Fig. 3C)—an observation that further explains how the pulses make our Slinky-robot move. Second, we find that for $A_{in} = 100$ mm, the excited waves propagate while maintaining

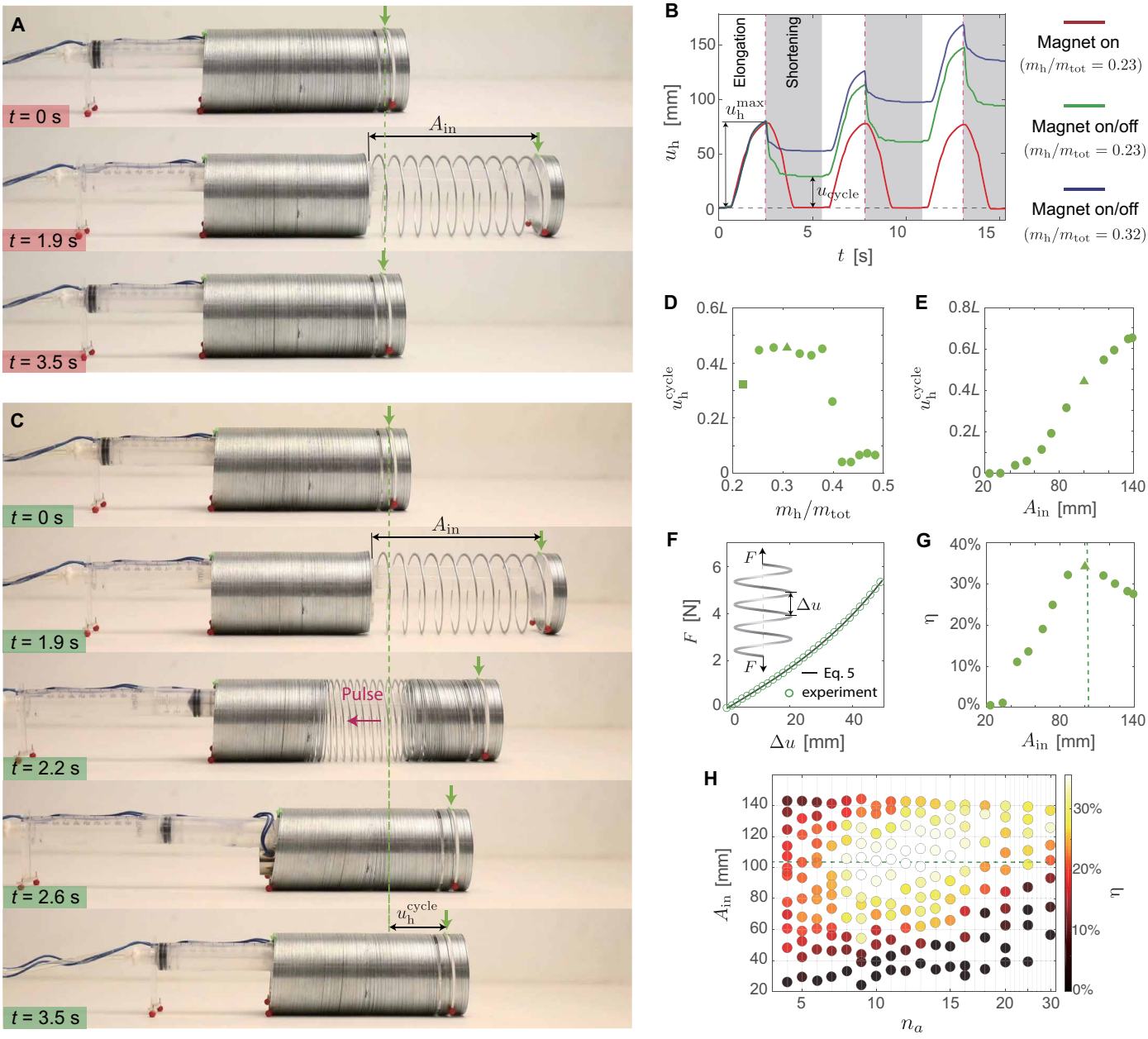


**Fig. 2. Performance of the Slinky-robot.** (**A**) Snapshots taken during a test in which we extend the front 10 loops to $A_{in}$ = 100 mm while keeping the electromagnet on. (**B**) Displacement of the head during three cycles for tests in which (i) $m_h/m_{tot}$ = 0.23 and we keep the electromagnet on (red line), (ii) $m_h/m_{tot}$ = 0.23 and we turn off the electromagnet after stretching (green line), and (iii) $m_h/m_{tot}$ = 0.32 and we turn off the electromagnet after stretching (blue line). (**C**) Snapshots taken during a test in which $A_{in}$ = 100 mm and we turn the electromagnet off after stretching the front loops. (**D**) Evolution of $u_h^{cycle}$ as a function of $m_h/m_{tot}$ for tests in which $A_{in}$ = 100 mm. The square and triangular markers correspond to $m_h/m_{tot}$ = 0.23 and 0.32, respectively. (**E**) Evolution of $u_h^{cycle}$ as a function of $A_{in}$ for tests in which $m_h/m_{tot}$ = 0.32. The triangular marker corresponds to $A_{in}$ = 100 mm. (**F**) Static response of the Slinky as measured in a uniaxial test. (**G**) Evolution of η as a function of $A_{in}$ for tests in which $m_h/m_{tot}$ = 0.32. The triangular markers correspond to $A_{in}$ = 100 mm. The green dashed line corresponds to the amplitude of the supported soliton, $A_s$. (**H**) Evolution of η as a function of $n_a$ and $A_{in}$ for tests in which $m_h/m_{tot}$ = 0.32. Photo credit: Bolei Deng, Harvard University.

their shape at a constant velocity of 279 loop/s, with only slight acceleration near the end due to boundary effects (Fig. 3D). This suggests that the Slinky supports the propagation of large-amplitude solitary waves. To further confirm this observation, we calculate the cross-correlation of the velocity signals measured at the 10th and 80th loops (Fig. 3E). We find that the cross-correlation is maximum and approaches unity for $A_{in}$ = 100 mm (movie S4), the same amplitude that maximizes the efficiency of our Slinky-robot (see Fig. 2G).

To provide deeper insight into these experimental results, we developed a mathematical model based on a one-dimensional array of concentrated masses $m$ connected by nonlinear springs, which represent the mass and elasticity of an individual loop, respectively

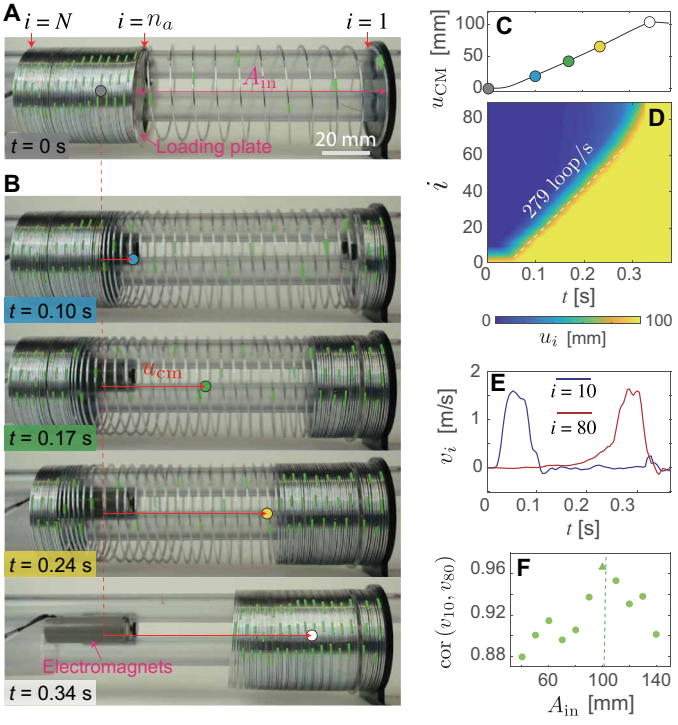


**Fig. 3. Wave propagation in the Slinky.** (**A**) Experimental setup used to test the propagation of pulses in the metallic Slinky. At $t = 0$ s, $n_a = 10$ loops between the loading plate and the front of the Slinky are stretched to $A_{in} = 100$ mm. (**B**) Snapshots of the propagation of the pulse in the Slinky at $t = 0.10$, 0.17, 0.24, and 0.34 s. The circular markers indicate the positions of the center of mass of the Slinky. (**C**) Displacement of the center of mass of the Slinky, $u_{CM}$, as a function of time. Circular markers correspond to the time points considered in (A) and (B). (**D**) Spatiotemporal displacement diagram of the propagating pulse. (**E**) Velocity signals measured at the 10th and 80th loops. (**F**) Evolution of the cross-correlation of $v_{10}(t)$ and $v_{80}(t)$ as a function of the input amplitude $A_{in}$. The triangular marker corresponds to $A_{in} = 100$ mm. The green dashed line corresponds to the amplitude of the supported soliton, $A_s$, predicted by Eq. 10. Photo credit: Bolei Deng, Harvard University.

(Fig. 4A). The governing equations for such discrete system can be written as

$$m\frac{\partial^2 u_i}{\partial t^2} = F(u_{i+1} - u_i) - F(u_i - u_{i-1}) \tag{4}$$

where $u_i$ represents the displacement of $i$th mass and $F(u_{i+1} - u_i)$ denotes the force in the spring connecting the $i$th and $(i + 1)$th masses. For the Slinky considered in this study, $m = 1.01$ g and the elastic response of an individual loop can be nicely fitted by

$$F(u_{i+1} - u_i) = k[(u_{i+1} - u_i) + \alpha(u_{i+1} - u_i)^3] \tag{5}$$

with a stiffness constant $k = 79.2$ N/m and a cubic nonlinearity parameter $\alpha = 155.1\ \mathrm{m}^{-2}$ (see Fig. 2F and section S3 for details). Note that Eq. 5 only captures the response of the Slinky under tension (i.e., $u_{i+1} - u_i \geq 0$) and therefore limits us to investigate rarefaction wave solutions.

Next, because in our experiments the wavelength of the propagating waves is much wider than a single loop, we take the continuum limit of Eq. 4 and retain derivatives up to fourth order to obtain the continuum governing equation

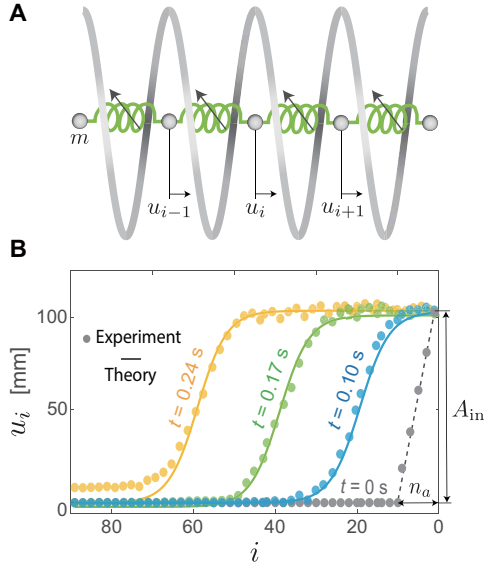


**Fig. 4. Mathematical model.** (**A**) Schematic of our model. Each nonlinear spring represents the elastic response of an individual loop, whereas each concentrated mass represents its mass. (**B**) Spatial displacement profiles at $t = 0$, 0.10, 0.17, and 0.24 s as measured in our experiments (circular markers) and predicted by our analytical solution given by Eq. 7 (solid lines).

$$\frac{1}{c_0^2}\frac{\partial^2 u}{\partial t^2} = \frac{\partial^2 u}{\partial \xi^2} + \frac{1}{12}\frac{\partial^4 u}{\partial \xi^4} + \alpha\frac{\partial}{\partial \xi}\left(\frac{\partial u}{\partial \xi}\right)^3 \tag{6}$$

where $u(\xi, t)$ is a continuous function that interpolates $u_i(t)$, i.e., $u(\xi = i, t) = u_i(t)$, $\xi$ denotes the loop number, and $c_0 = \sqrt{k/m} = 280.0$ m/s is the velocity of linear waves in the long-wavelength regime. Equation 6 has been shown to be equivalent to the generalized Boussinesq equation and admits an analytical solution in the form of a rarefaction solitary wave (*32*)

$$u = -\sqrt{\frac{2}{3\alpha}}\arctan\left[\tanh\left(\frac{\xi - \xi_0 - c\,t}{W}\right)\right] + \frac{\pi}{4}\sqrt{\frac{2}{3\alpha}} \tag{7}$$

with

$$W = \sqrt{\frac{1}{3(c^2/c_0^2 - 1)}} \tag{8}$$

where $\xi_0$ identifies the position of the wave at $t = 0$ and $c$ and $W$ are the velocity and the characteristic width of the pulse, respectively. Because solitary waves propagate maintaining their shape, we require the maximum extension in the Slinky [i.e., max $(\partial u/\partial \xi)$] to be equal to that imposed to the 10 loops before turning off the electromagnets (i.e., $A_{in/na}$)

$$\frac{A_{in}}{n_a} = \max\left(\frac{\partial u}{\partial \xi}\right) = \sqrt{\frac{2}{\alpha}\left(\frac{c^2}{c_0^2} - 1\right)} \tag{9}$$

and in this way obtain a relation between propagation velocity $c$ and the applied input $A_{in}$. Last, the amplitude of the supported soliton can be calculated as

$$A_s = u(\xi \to \infty) - u(\xi \to -\infty) = \frac{\pi}{\sqrt{6\alpha}} \tag{10}$$

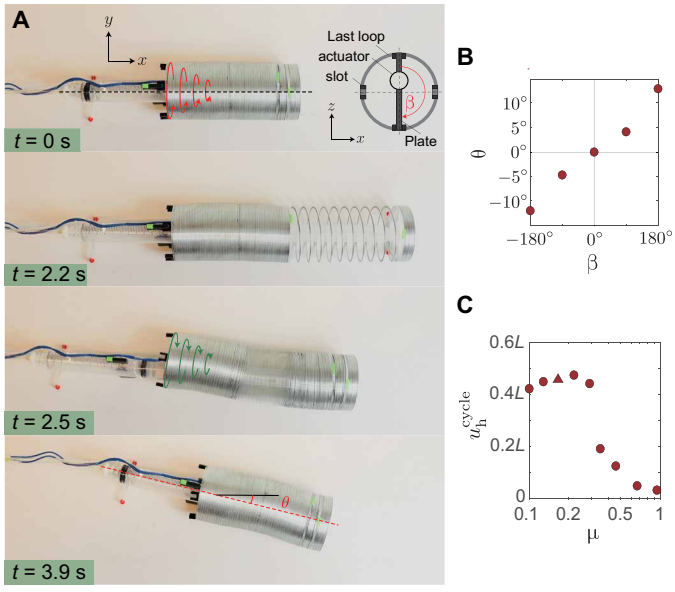


**Fig. 5. Steering and moving over different surfaces.** (**A**) Snapshots taken during a test in which we twist the last loop by β = 180° before initiating the wave. The Slinky-robot steers by an angle θ = 13° when the pulse reaches its tail. (**B**) Evolution of the steering angle θ as a function of the applied twist β. (**C**) Evolution of $u_h^{cycle}$ as a function of the friction coefficient between the Slinky and the substrate, μ. The triangular marker corresponds to Bristol paper—the substrate considered in Fig. 2. Photo credit: Bolei Deng, Harvard University.

and is found to be an intrinsic property of the Slinky, because it only depends on α (i.e., on the strength of the nonlinear term in its static force-displacement response; see Eq. 5). For the Slinky considered in this study, using Eqs. 8 to 10, we obtain $A_s$ = 103 mm, $c$ = 282.2 loop/s, and $W$ = 4.62 loop—values that match extremely well with the experimental results (Fig. 4B). Note that the model also confirms the experimental observations reported in Fig. 3, as it predicts that only pulses with amplitude $A_{in} \sim A_s$ = 103 mm propagate in solitary fashion through the Slinky. Last, our analysis reveals that the efficiency of the Slinky-robot is maximum when the initiated waves are solitons (i.e., when $A_{in} = A_s$; see green dashed lines in Fig. 2, G and H). The nondispersive nature and compactness of solitary pulses make them extremely efficient in transferring the energy provided by the pneumatic actuator to motion, ultimately resulting in the most efficient pulse-driven locomotion.

## DISCUSSION

To summarize, we have shown that backward propagating solitons can be harnessed to efficiently make a Slinky-robot move forward. Although limbless organisms have recently inspired the design of a variety of robots (*33*–*40*), to the best of our knowledge, this is first robotic system that exploits elastic pulses to move. It is also worth noting that the principles presented in this study are different from those used by ultrasonic motors (*19*). Our Slinky-robot is flexible and uses nonlinear pulse waves to change the position of the center of mass. By contrast, ultrasonic motors are powered by linear sinusoidal waves, induce local microscopic displacements (eventually adding up over many periods to produce a large motion), and modulate friction by exerting an oscillating normal force between stiff surfaces.

It is important to point out that, while in this study we have focused on rectilinear forward crawling, the flexibility of the Slinky can be exploited to expand the range of achievable motions. For example, we can make the robot steer by twisting the last loop at the back of the robot by an angle β before initiating the wave (Fig. 5A and movie S5) and easily control the steering angle θ by tuning both the direction and magnitude of β (Fig. 5B).

We also want to emphasize that our robot can move over a broad range of surfaces. To demonstrate this point, in Fig. 5C, we report $u_h^{cycle}$ recorded when our Slinky-robot (with $m_h/m_{tot}$ = 0.32 and $A_{in}$ = 100 mm) moves on surfaces characterized by a broad range of roughness (so that μ ∈ [0.1,1]). Notably, we find that for a μ < 0.3, $u_h^{cycle}$ remains almost constant ($u_h^{cycle} \sim 0.45L$). For larger values of μ, the frictional forces prevent propagation of the pulses and $u_h^{cycle}$ drops significantly—an additional demonstration of the important role played by the wave propagation in achieving locomotion (movie S6).

Last, while in this study we have used a Slinky to realize such pulse-driven locomotion, the principles are general and can be expanded to a broad range of stretchable systems across scales, opening avenues even for microscale crawlers suitable for medical applications.

## MATERIALS AND METHODS

The basic properties of the metallic Slinky are provided in section S1. Details on fabrication, testing, and additional results of the Slinky-robot are described in section S2. Details on the experiments conducted to characterize the propagation of nonlinear waves are presented in section S3. Details on the model established to characterize the propagation of nonlinear waves are presented in section S4.

## SUPPLEMENTARY MATERIALS

Supplementary material for this article is available at http://advances.sciencemag.org/cgi/content/full/6/18/eaaz1166/DC1

## REFERENCES AND NOTES

1. P. M. Reis, A perspective on the revival of structural (in) stability with novel opportunities for function: From buckliphobia to buckliphilia. *J. Appl. Mech.* **82**, 111001 (2015).
2. K. Bertoldi, V. Vitelli, J. Christensen, M. van Hecke, Flexible mechanical metamaterials. *Nat. Rev. Mater.* **2**, 17066 (2017).
3. D. P. Holmes, Elasticity and stability of shape-shifting structures. *Curr. Opin. Colloid Interface Sci.* **40**, 118–137 (2019).
4. B. Deng, J. Raney, V. Tournat, K. Bertoldi, Elastic vector solitons in soft architected materials. *Phys. Rev. Lett.* **118**, 204102 (2017).
5. B. Deng, P. Wang, Q. He, V. Tournat, K. Bertoldi, Metamaterials with amplitude gaps for elastic solitons. *Nat. Commun.* **9**, 3410 (2018).
6. B. Deng, V. Tournat, K. Bertoldi, Effect of predeformation on the propagation of vector solitons in flexible mechanical metamaterials. *Phys. Rev. E* **98**, 053001 (2018).
7. J. R. Raney, N. Nadkarni, C. Daraio, D. M. Kochmann, J. A. Lewis, K. Bertoldi, Stable propagation of mechanical signals in soft media using stored elastic energy. *Proc. Natl. Acad. Sci. U.S.A.* **113**, 9722–9727 (2016).
8. N. Nadkarni, A. F. Arrieta, C. Chong, D. M. Kochmann, C. Daraio, Unidirectional transition waves in bistable lattices. *Phys. Rev. Lett.* **116**, 244501 (2016).
9. B. Deng, P. Wang, V. Tournat, K. Bertoldi, Nonlinear transition waves in free-standing bistable chains. *J. Mech. Phys. Solids* **136**, 103661 (2019).
10. H. Yasuda, Y. Miyazawa, E. G. Charalampidis, C. Chong, P. G. Kevrekidis, J. Yang, Origami-based impact mitigation via rarefaction solitary wave creation. *Sci. Adv.* **5**, eaau2835 (2019).
11. B. Deng, Y. Zhang, Q. He, V. Tournat, P. Wang, K. Bertoldi, Propagation of elastic solitons in chains of pre-deformed beams. *New J. Phys.* **21**, 073008 (2019).
12. J. Vila, G. H. Paulino, M. Ruzzene, Role of nonlinearities in topological protection: Testing magnetically coupled fidget spinners. *Phys. Rev. B* **99**, 125116 (2019).
13. Y. Xia, M. Ruzzene, A. Erturk, Dramatic bandwidth enhancement in nonlinear metastructures via bistable attachments. *Appl. Phys. Lett.* **114**, 093501 (2019).

14. B. Deng, C. Mo, V. Tournat, K. Bertoldi, J. R. Raney, Focusing and mode separation of elastic vector solitons in a 2D soft mechanical metamaterial. *Phys. Rev. Lett.* **123**, 024101 (2019).
15. W. Jiao, S. Gonella, Intermodal and subwavelength energy trapping in nonlinear metamaterial waveguides. *Phys. Rev. Appl.* **10**, 024006 (2018).
16. D. M. J. Dykstra, J. Busink, B. Ennis, C. Coulais, Viscoelastic snapping metamaterials. *J. Appl. Mech.* **86**, 111012 (2019).
17. W. B. Yapp, B. I. Roots, Locomotion of worms. *Nature* **177**, 614–616 (1956).
18. K. J. Quillin, Kinematic scaling of locomotion by hydrostatic animals: Ontogeny of peristaltic crawling by the earthworm lumbricus terrestris. *J. Exp. Biol.* **202**, 661–674 (1999).
19. S. Ueha, Y. Tomikawa, M. Kurosawa, N. Nakamura, *Ultrasonic Motors: Theory and Applications* (Clarendon Press, 1993).
20. T. Sashida, T. Kenjo, *An Introduction to Ultrasonic Motors* (Oxford Univ. Press, 1993).
21. H. Imabayashi, T. Fujimura, T. Funakubo, Ultrasonic motor. US Patent 5,357,164 (1994).
22. N. W. Hagood, A. J. McFarland, Modeling of a piezoelectric rotary ultrasonic motor. *IEEE Trans. Ultrason. Ferroelectr. Freq. Control* **42**, 210–224 (1995).
23. D. P. Holmes, A. D. Borum, B. F. Moore III, R. H. Plaut, D. A. Dillard, Equilibria and instabilities of a slinky: Discrete model. *Int. J. Non-Lin. Mech.* **65**, 236–244 (2014).
24. J. M. Bowen, Slinky oscillations and the notion of effective mass. *Am. J. Phys.* **50**, 1145–1148 (1982).
25. A.-P. Hu, A simple model of a slinky walking down stairs. *Am. J. Phys.* **78**, 35–39 (2010).
26. M. S. Longuet-Higgins, On Slinky: The dynamics of a loose, heavy spring. *Math. Proc. Camb. Philos. Soc.* **50**, 347–351 (1954).
27. M. Remoissenet, *Waves Called Solitons* (Springer-Verlag Berlin Heidelberg, 1999).
28. T. Dauxois, M. Peyrard, *Physics of Solitons* (Cambridge Univ. Press, 2006).
29. R. Zaera, J. Vila, J. Fernandez-Saez, M. Ruzzene, Propagation of solitons in a two-dimensional nonlinear square lattice. *Int. J. Non-Lin. Mech.* **106**, 188–204 (2018).
30. M. I. Hussein, M. J. Leamy, M. Ruzzene, Dynamics of phononic materials and structures: Historical origins, recent progress, and future outlook. *Appl. Mech. Rev.* **66**, 040802 (2014).
31. J. Chang, D. Wei, J. W. Fisher III, A video representation using temporal superpixels, in *2013 IEEE Conference on Computer Vision and Pattern Recognition* (IEEE, 2013), pp. 2051–2058.
32. S. N. Pnevraatikos, Solitons in nonlinear atomic chains. *North-Holland Math. Stud.* **103**, 397–437 (1985).
33. D. Rus, M. T. Tolley, Design, fabrication and control of soft robots. *Nature* **521**, 467–475 (2015).
34. A. Rafsanjani, Y. Zhang, B. Liu, S. M. Rubinstein, K. Bertoldi, Kirigami skins make a simple soft actuator crawl. *Sci. Robot.* **3**, eaar7555 (2018).
35. C. D. Onal, D. Rus, Autonomous undulatory serpentine locomotion utilizing body dynamics of a fluidic soft robot. *Bioinspir. Biomim.* **8**, 026003 (2013).
36. S. Seok, C. D. Onal, K.-J. Cho, R. J. Wood, D. Rus, S. Kim, Meshworm: A peristaltic soft robot with antagonistic nickel titanium coil actuators. *IEEE/ASME Trans. Mechatron.* **18**, 1485–1497 (2013).
37. K. Jung, J. C. Koo, J. D. Nam, Y. K. Lee, H. R. Choi, Artificial annelid robot driven by soft actuators. *Bioinspir. Biomim.* **2**, S42–S49 (2007).
38. A. B. Slatkin, J. Burdick, W. Grundfest, The development of a robotic endoscope, in *Proceedings of the 1995 IEEE/RSJ International Conference on Intelligent Robots and Systems. Human Robot Interaction and Cooperative Robots* (IEEE, 1995), vol. 2, pp. 162–171.
39. E. V. Mangan, D. A. Kingsley, R. D. Quinn, H. J. Chiel, Development of a peristaltic endoscope, in *Proceedings of the 2002 IEEE International Conference on Robotics and Automation (Cat. No. 02CH37292)* (IEEE, 2002), vol. 1, pp. 347–352.
40. J. Aguilar, T. Zhang, F. Qian, M. Kingsbury, B. McInroe, N. Mazouchova, C. Li, R. Maladen, C. Gong, M. Travers, R. L. Hatton, H. Choset, P. B. Umbanhowar, D. I. Goldman, A review on locomotion robophysics: The study of movement at the intersection of robotics, soft matter and dynamical systems. *Rep. Prog. Phys.* **79**, 110001 (2016).



**Acknowledgments**

**Funding:** K.B. acknowledges support from the NSF under grant no. DMR-1420570 and from the Army Research Office under grant no. W911NF-17-1-0147. V.T. acknowledges support from project Acoustics hub funded by Region Pays de la Loire. The views and conclusions contained in this document are those of the authors and should not be interpreted as representing the official policies, either expressed or implied, of the Army Research Laboratory or the U.S. government. The U.S. government is authorized to reproduce and distribute reprints for government purposes notwithstanding any copyright notation herein. **Author contributions:** B.D., V.T., and K.B. came up with the initial idea. B.D. and K.B. designed and supervised the research. B.D. and L.C. performed the experiments. B.D. and D.W. analyzed the experimental data. B.D. developed the theoretical model. All authors contributed in writing the manuscript. **Competing interests:** The authors declare that they have no competing interests. **Data and materials availability:** All data needed to evaluate the conclusions in the paper are present in the paper and/or the Supplementary Materials. Additional data related to this paper may be requested from the authors.

Submitted 13 August 2019
Accepted 17 January 2020
Published 1 May 2020
10.1126/sciadv.aaz1166

**Citation:** B. Deng, L. Chen, D. Wei, V. Tournat, K. Bertoldi, Pulse-driven robot: Motion via solitary waves. *Sci. Adv.* **6**, eaaz1166 (2020).

Science Advances

# Pulse-driven robot: Motion via solitary waves

Bolei Deng, Liyuan Chen, Donglai Wei, Vincent Tournat and Katia Bertoldi

*Sci Adv* **6** (18), eaaz1166.
DOI: 10.1126/sciadv.aaz1166



*Science Advances* (ISSN 2375-2548) is published by the American Association for the Advancement of Science, 1200 New York Avenue NW, Washington, DC 20005. The title *Science Advances* is a registered trademark of AAAS.

Science Advances
AAAS

advances.sciencemag.org/cgi/content/full/6/18/eaaz1166/DC1

# Supplementary Materials for

## Pulse-driven robot: Motion via solitary waves

Bolei Deng, Liyuan Chen, Donglai Wei, Vincent Tournat, Katia Bertoldi*

*Corresponding author. Email: bertoldi@seas.harvard.edu

Published 1 May 2020, *Sci. Adv.* **6**, eaaz1166 (2020)
DOI: 10.1126/sciadv.aaz1166

**The PDF file includes:**



**Other Supplementary Material for this manuscript includes the following:**

(available at advances.sciencemag.org/cgi/content/full/6/18/eaaz1166/DC1)

# 1 Our flexible structure: a Slinky

All experiments presented in this study are are conducted using metal Slinkys (Amazon Standard Identification Number (ASIN): B06XS1SNT1) with $N = 90$ loops, mass $m_{\text{Slinky}} = 90.8$ g (so that the mass of each loop is $m = m_{\text{Slinky}}/N = 1.009$ g), inner radius of $43.13$ mm, outer radius of $46.58$ mm and thickness of $0.54$ mm ( Fig. S1).

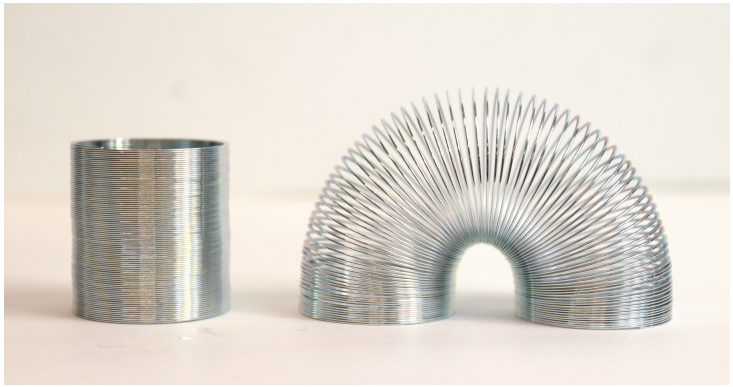

*Figure S1: Two snapshots of the metal Slinky used in this study. Photo Credit: Bolei Deng, Harvard University.*

## 1.1 Static response

To characterize the static response of the Slinky, we conduct uniaxial tests using a single-axis Instron (Instron 5566) equipped with a 2 kN load cell. More specifically, we cut a segment comprising 4 loops from the Slinky and fix its ends to two acrylic plates that are connected to the Instron (Fig. S2*)*. We then apply a displacement $u_{\text{applied}} = 200$ mm at a rate of 2 mm/s (see Fig. S2*A*) and monitor the force $F$. In Fig. S2*B* we report the evolution of $F$ as a function of the average extension of a loop, $\Delta u = u_{\text{applied}}/4$. We find that the force-displacement curve is non-linear, with the Slinky that becomes stiffer for increasing values of applied displacement. This response is nicely captured using

$$F = k(\Delta u + \alpha\, \Delta u^3), \tag{S1}$$

with $k = 79.2\,\text{N/m}$ and $\alpha = 155.1\,\text{m}^{-2}$.

## 1.2 Friction coefficient

We conduct a set of tests to measure the frictional force when the Slinky move on different substrates, including paper, wood, teflon, steel, acrylic, foam and sand paper. Specifically, in these experiments the Slinky is placed on a surface and pushed (i.e. moved in forward direction) for 2 cm at a constant speed of 2 mm/s using a motorized translation stage (LTS300 - Thorlabs) which is attached to the Slinky via a plastic bar (Fig. S3). The resistive force (i.e. the friction force), $F_{\text{fr}}$, is measured using a 1 lb Load Cell (LSB200 Miniature S-Beam Load Cell, FUTEK Advanced Sensor Technology, Inc.). The friction coefficient $\mu$ is then extracted from our force measurements as

$$\mu = \frac{< F_{\text{fr}} >}{\left(m_{\text{Slinky}} + m_{\text{bar}}\right) g} \tag{S2}$$

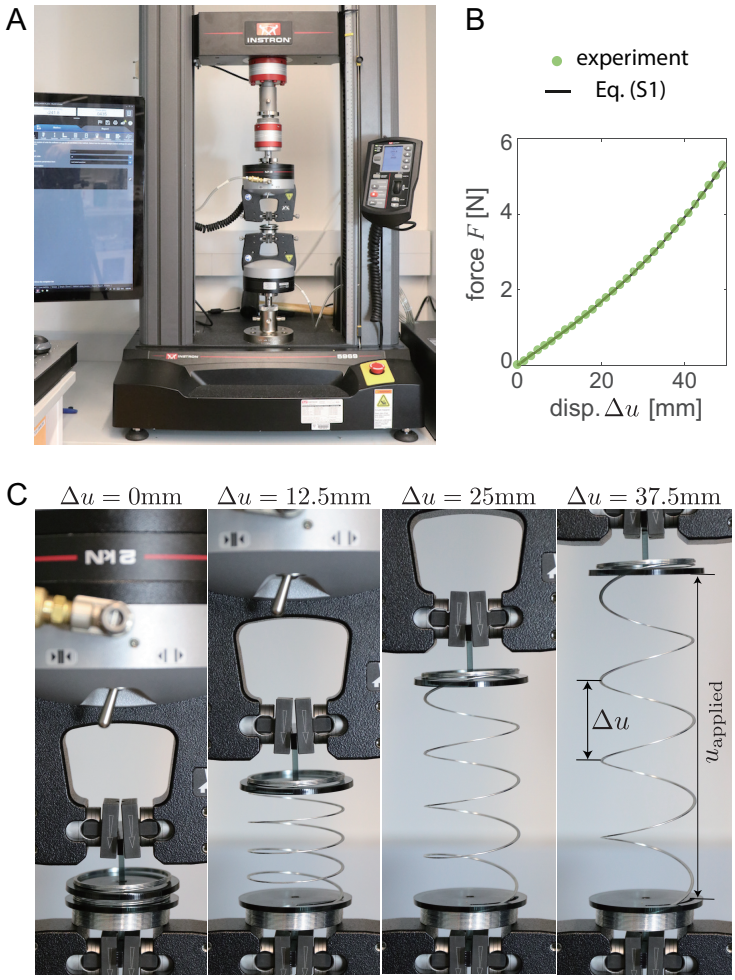


*Figure S2: Static tests. (A) Our testing setup. (B) Quasi-static force-displacement ($F$-$\Delta u$) response for the Slinky as measured in the experiment (markers) and captured by Eq. (S1) (line). (C) Snapshots of the Slinky at different level of applied deformation. Photo Credit: Bolei Deng, Harvard University.*

where $< \cdot >$ denotes the mean value, $m_{\text{bar}} = 0.2$ g is the mass of the plastic bar and $g = 9.8$ m/s$^2$. In Table S1 we report the obtained friction coefficients between the Slinky and the substrates considered in this study.

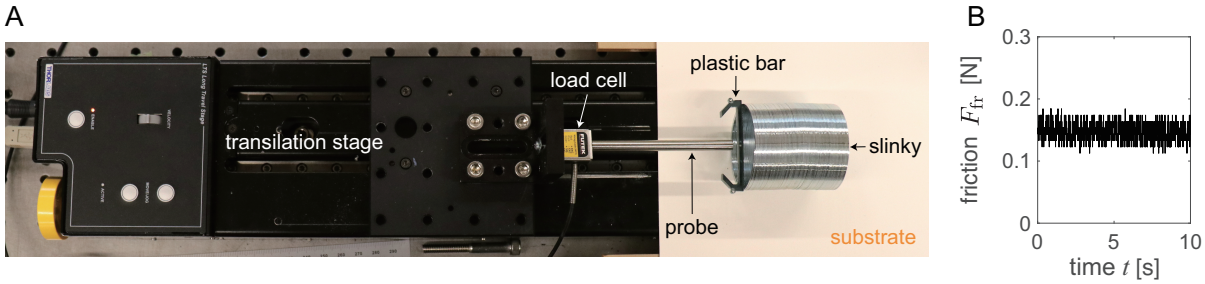


*Figure S3: Friction test. (A) Components of the experimental setup used to measure the frictional properties of our Slinky with different substrates. (B) Friction force $F_{fr}$ recorded when pushing the Slinky on the substrate. Photo Credit: Bolei Deng, Harvard University.*

| substrate | friction coefficient $\mu$ |
|---|---|
| Teflon resin (VWR International, Radnor, PA) | 0.10 |
| Polished wood (McMaster-Carr part number: 5168T7) | 0.13 |
| Paper (Bristol Pad 19×24 in, Canson, Annonay, France) | 0.17 |
| Acrylic plate (McMaster-Carr part number: 8505K722) | 0.22 |
| Stainless steel (McMaster-Carr part number: 8983K221) | 0.27 |
| Acrylic plate (McMaster-Carr part number: 8505K722) | 0.35 |
| Foam (McMaster-Carr part number: 8643K544) | 0.46 |
| Sand paper (Grit 320, McMaster-Carr part number: 4680A6) | 0.68 |
| Sand paper (Grit 120, McMaster-Carr part number: 4681A4) | 0.95 |

**Table S1.** Friction coefficient between the Slinky and the substrates considered in this study.

# 2 Our Slinky-robot

## 2.1 Fabrication

As shown in Fig. S4, our Slinky robot comprises ($i$) a Slinky; ($ii$) an electromagnet (12V DC 20N, UXCELL) and an acrylic plate with one metallic nut fixed on it to initiate the pulse (note that the plate remains attached to the electromagnet when the magnetic field is on); ($iii$) a plastic syringe (realized by by concatenating two 10 mL syringes) to elongate the front part of the Slinky; ($iv$) an acrylic front plate to connect the Slinky to the syringe; and ($v$) an acrylic back plate to support the rear of the syringe (note that two rounded pins are glued to its bottom using Krazy Glue to minimize friction with the surface). Note that all plates are laser cut from acrylic sheets with thickness of 2 mm and that several red plastic spheres are glued on to the Slinky to prevent it from rolling.

To assemble the Sklinky robot we take the following steps (Fig. S4):

- **Step A:** we connect the acrylic back plate to the syringe using a circular hole embedded in the plate and glue (using Krazy Glue - Elmer) the electromagnet to the right end of the syringe barrel.
- **Step B:** we glue the front plate to the 20-th loop of the Slinky and the loading plate to the $20 + n_a$-th loop (note that in this study we consider $n_a \in [4, 30]$). Note that the shape of the two plates is designed to perfectly fit the loops as well as to avoid contact with the ground.
- **Step C:** we glue the head of the syringe to the front plate. Note that the syringe is supported both by the front and back plates.

## 2.2 Actuation strategy

Our Slinky robot is actuated by cyclically inflating/deflating and the plastic syringe and turning on/off the electromagnet. Specifically (Fig. S5 and Movie S1),

- **Step 1:** we inflate the syringe while keeping the electromagnet on to stretch the $n_a$ loop located between the front and loading plates.
- **Step 2:** we turn the electromagnet off to initiate a non-linear pulse that propagate toward the back of the Slinky (because of the pre-stretch in the first $n_a$ loops of the Slinky, the loading plate starts to move towards the front plate when the magnetic filed is turned off, exciting a non-linear wave).
- **Step 3:** we deflate the syringe to bring the electromagnet back in contact with the loading plate.

Given the simplicity of our robot, an open-loop control strategy is used for its operation. The control system consists of a micro-controller unit (model ATmega2560, Arduino Mega2560) that turns on and off the electromagnet as well as opens and closes two pneumatic solenoid valves (X-Valve, Parker Co.) to inflate and deflate the syringe (Fig. S6).

## 2.3 Efficiency

The efficiency $\eta$ of our Slinky-robot can be calculated as

$$\eta = \frac{W_{\text{req}}}{W_{\text{in}}}, \tag{S3}$$

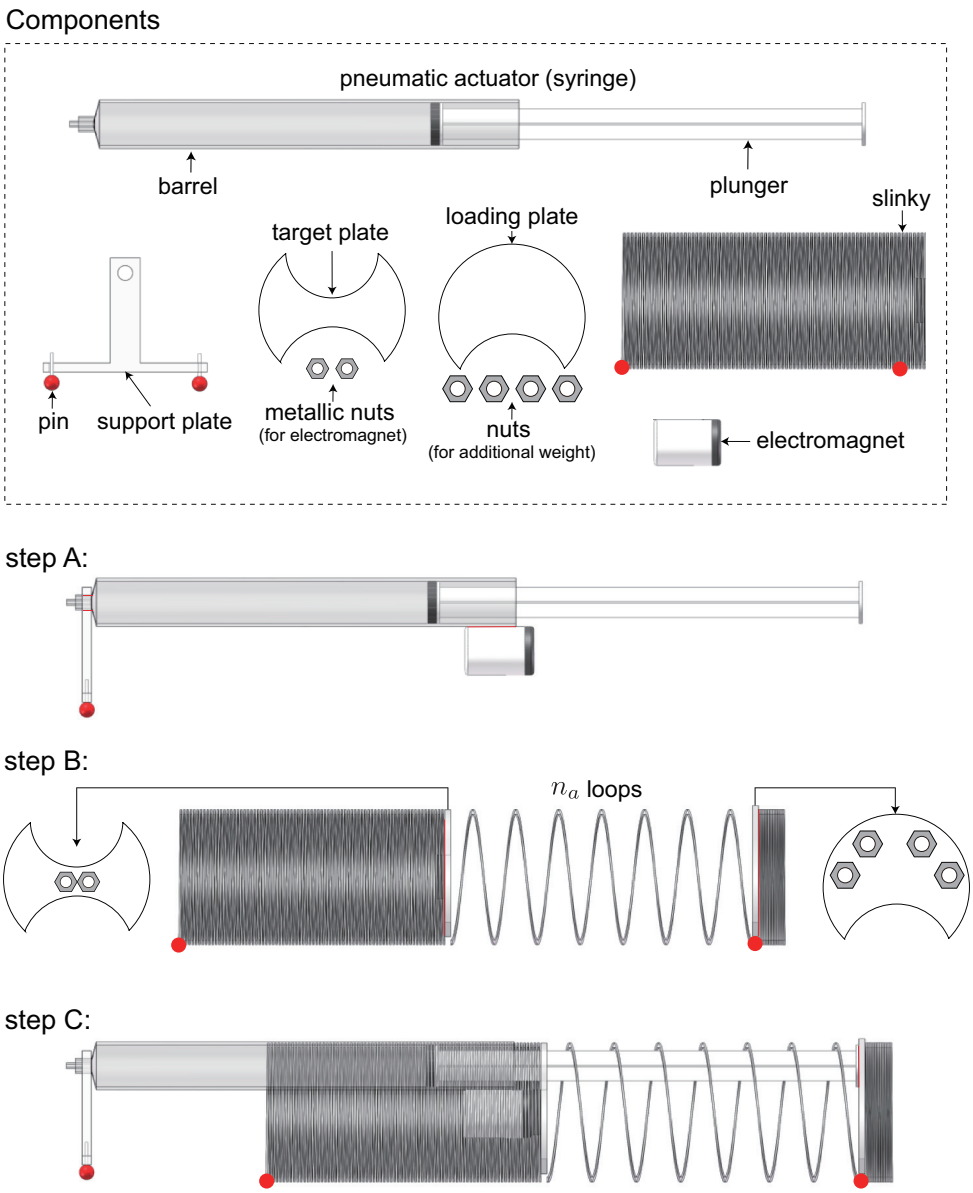


*Figure S4: Components and assembly of our Slinky-robot.*

where $W_{\text{req}}$ denotes the work done by the robot to move on the substrate and $W_{\text{in}}$ is the work supplied to initiate the pulse. More specifically, $W_{\text{in}}$ is the work done by the syringe to extend the front $n_a$ loops of the Slinky to $A_{\text{in}}$ and to move the head of the Slinky

$$W_{\text{in}} = \mu\, m_{\text{h}} g\, u_{\text{h}}^{\max} + n_a \int_0^{A_{\text{in}}/n_a} F\,(\Delta u)\,\mathrm{d}\Delta u \tag{S4}$$

where $g$ is the gravitational constant, $F$ denotes the force required to stretch one loop of the slinky by $\Delta u$, $\mu$ is the friction coefficient between the Slinky and the substrate, $m_{\text{h}}$ is the mass of the head of the

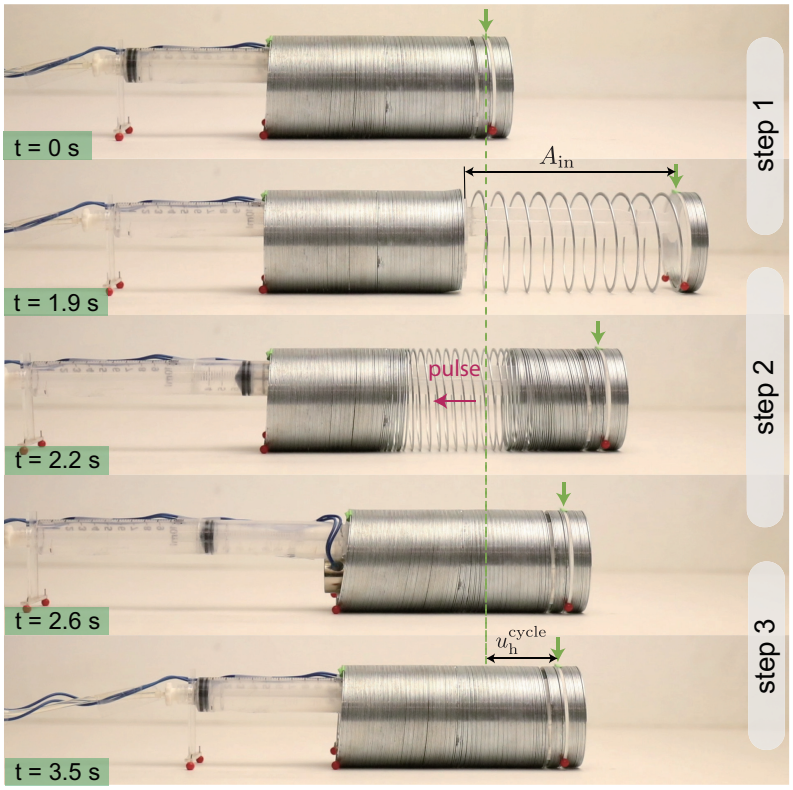


*Figure S5: Actuation of our Slinky-robot.*

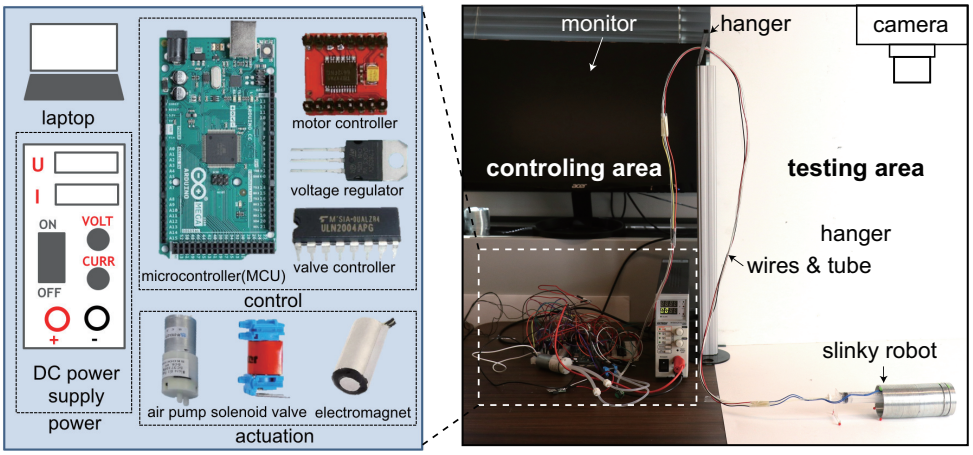


*Figure S6: Components used to actuate and control our Slinky-robot. Photo Credit: Bolei Deng, Harvard University.*

robot and $u_{\mathrm{h}}^{\mathrm{max}}$ is the maximal displacement of the head of the Slinky in each cycle. By substituting

Eq. (S1) into Eq. (S4) we obtain

$$W_{\text{in}} = \mu\, m_{\text{h}} g\, u_{\text{h}}^{\max} + \frac{k A_{\text{in}}^2}{n_a}\left(1 + \frac{\alpha A_{\text{in}}^2}{2 n_a^2}\right). \tag{S5}$$

where Moreover, $W_{\text{req}}$ is given by

$$W_{\text{req}} = \mu\, m_{\text{tot}} g\, u_{\text{h}}^{\text{cycle}}, \tag{S6}$$

where $m_{\text{tot}}$ is the total mass of the Slinky robot and $u_{\text{h}}^{\text{cycle}}$ is the the difference between the displacement of the head at the end and at the beginning of a specific cycle.

## 2.4 Additional results

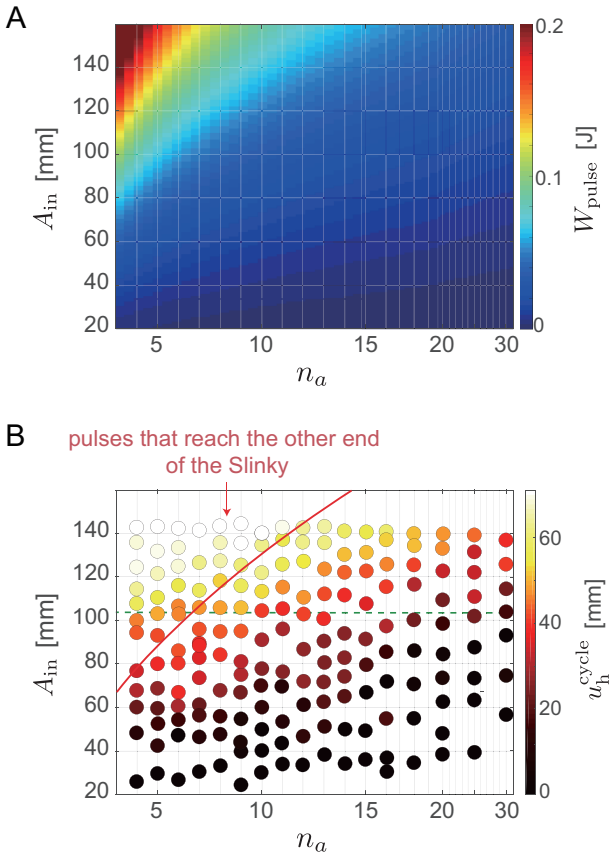


*Figure S7: Additional results. (A) Evolution of the energy carried by the elastic pulses, $W_{pulse}$, as a function of $n_a$ and $A_{in}$. The energy carried by the pulse is calculated as $W_{pulse} = n_a \int_0^{\frac{A_{in}}{n_a}} F(\Delta u)\, d\Delta u$. Small vales of $n_a$ and large values of $A_{in}$ produce pulses with higher energy. Large values of $n_a$ and small values of $A_{in}$ yields weak pulses that carry low energy. (B) Evolution of $u_h^{cycle}$ (i.e. the difference between the displacement of the head at the end and at the beginning of a specific cycle) for the experiments reported in Fig. 2H. For a given $A_{in}$, $u_h^{cycle}$ saturates when the energy carried by the pulses is large enough to make them reach the back of the Slinky. The red line indicates $A_{in}$-$n_a$ pairs for which $W_{pulse} = 0.05$ J.*

## 3 Propagation of non-linear waves: experiments

In this Section we describe the dynamic tests that we conducted to characterize the propagation of non-linear waves through the Slinky. As shown in Fig. S8, in these tests the Slinky is supported by a PETG rod (McMaster Carr product id: 9245K21) and has one of its ends is glued to a 3 mm thick acrylic plate (denoted as "front plate" in Fig. S8*A*). To initiate large amplitude waves, we use two electromagnets (McMaster Carr product id: 5698K7) glued to the PETG rod and an acrylic plate (denoted as "loading plate" in Fig. S8*B*) that has two metallic bolts glued to it and is placed between the 10-th and 11-th loops. When the magnetic field is on, the loading plate remains in contact with the electromagnet s, so that the $n_a$ loops between the loading and front plates can be pre-stretched by pushing the front plate to a distance $A_{\text{in}}$ from the loading plate using a plastic telescopic rod (see Fig. S8*A*). The pulse is then initiated by turning the electromagnets off. Because of the pre-stretch in the $n_a$ loops of the Slinky, the loading plate starts to move towards the front plate, exciting a non-linear wave that propagates towards the left in the Slinky. The propagation of the pulse wave through the Slinky is observed with a high-speed camera (SONY RX100) recording at 240 Hz with a pixel size of 0.11 mm/pixel and the displacement of the loops is determined by tracking the position of green markers attached to every other loop (see Fig. S8*B*) via a superpixel-based method implemented in MATLAB [Ref. 33 in main text].

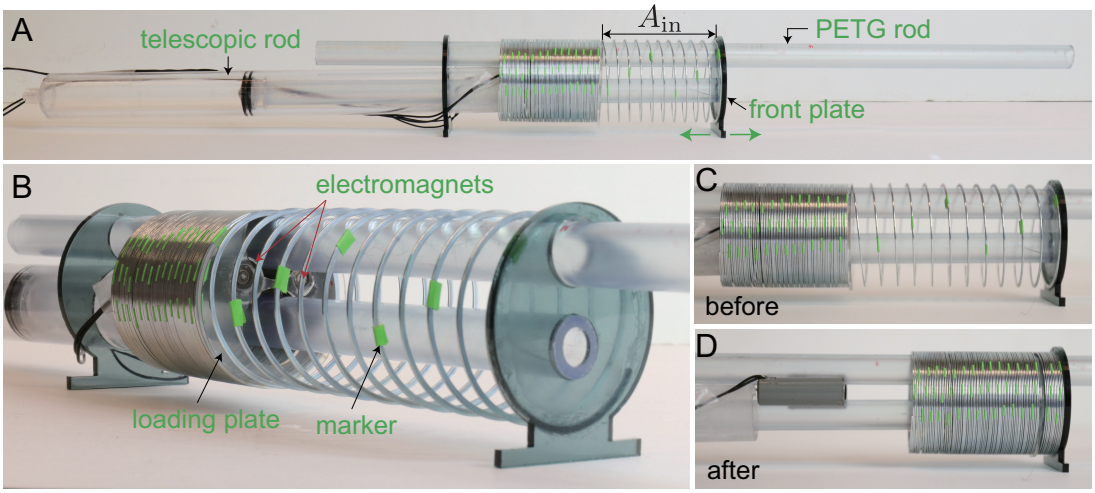


*Figure S8: Experimental setup used to study the propagation of non-linear waves in a Slinky. (A) Side view of the experimental setup. (B) 3D view of the experimental setup. $n_a = 10$ loops near the front of the Slinky are stretched when the electromagnet is on. Green paper markers are used to track the movement of every other loop during the propagation of the non-linear wave. (C) Zoomed-in side view of the Slinky before the initiation of the wave. The electromagnet is on, keeping the loading plate in place and enabling stretching of 10 loops at the front of the Slinky. (D) Zoomed-in side view of the Slinky after the non-linear wave has reached the left end of the structure. As a result of the wave propagation, the center of mass of the Slinky has moved forward. Photo Credit: Bolei Deng, Harvard University.*

In Fig. S9 we focus on 4 experiments in which $n_a = 10$, $A_{\text{in}} = 40$ mm, 80 mm, 100 mm and 120 mm and the pulse is initiated by turning the electromagnet off at $t = 0$ s. For each experiment we show the displacement of the loops along the chain, $u_i$, at $t = 0$ s (i.e. just before the electromagnet is turned off), 0.1 s, 0.17 s and 0.24 s. The plots clearly indicates that in all experiments there is a pulse

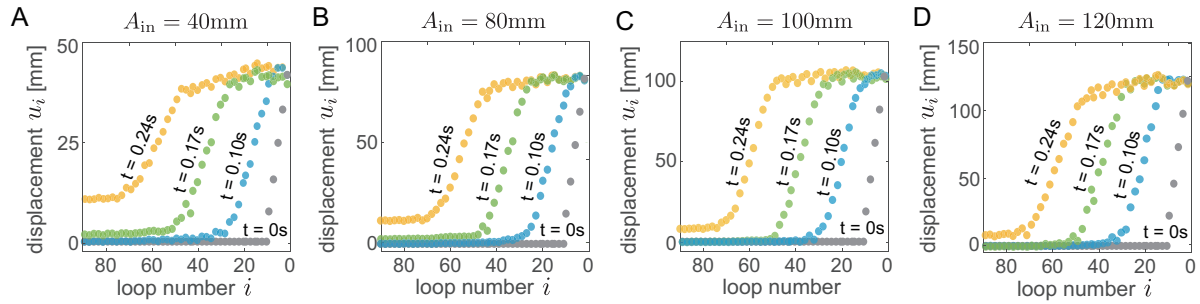


*Figure S9: Evolution of the displacement of the loops along the Slinky at $t = 0$ s (i.e. just before the electromagnet is tunrned off) 0.10 s, 0.17 s and 0.24 s for input amplitudes (A) $A_{in} = 40$ mm, (B) $A_{in} = 80$ mm, (C) $A_{in} = 100$ mm and (D) $A_{in} = 120$ mm.*

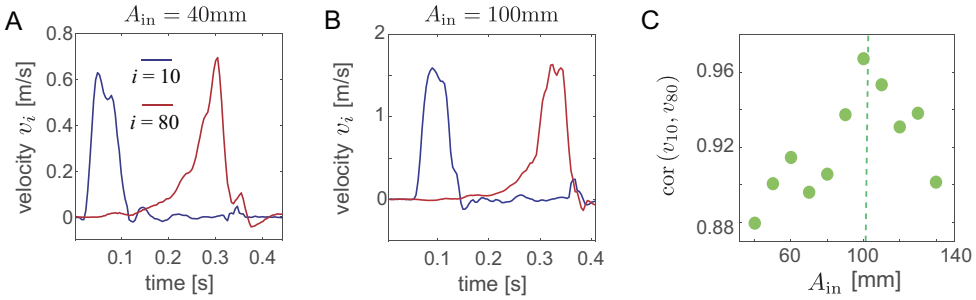


*Figure S10: Velocity signals and cross correlations. (A)-(B) Velocity signals measured at the 10-th and 80-th loops ($v_{10}(t)$ and $v_{80}(t)$) for the experiments with input amplitude (A) $A_{in} = 40$ mm and (B) $A_{in} = 100$ mm. (C) Evolution of the cross-correlation of $v_{10}(t)$ and $v_{80}(t)$ ($cor(v_{10}, v_{80})$) as a function of the input amplitude $A_{in}$.*

propagating through the Slinky. To get more insight into the characteristics of these pulses, we then compare the velocity signals measured at the 10-th and 80-th loops as a function of the input amplitude $A_{\rm in}$ (in Figs. S10*A* and *B* we report $v_{10}(t)$ and $v_{80}(t)$ for $A_{\rm in}$= 40 mm and 100 mm, respectively). As shown in Fig. S10*C*, we find that the cross-correlation of $v_{10}(t)$ and $v_{80}(t)$ is significantly affected by $A_{\rm in}$. Specifically, it approaches unity for $A_{\rm in}$ =100 mm and systematically decreases for both larger and smaller input amplitudes, suggesting that our system might support the propagation of solitary waves only for $A_{\rm in} \sim 100$ mm.

Next, to calculate the speed at which the pulse propagates, we determine the location of the pulse by identifying the loop $i_S$ that satisfies

$$i_S(t) = \min\, i, \quad \text{s.t. } u_i(t) > \frac{A_{\rm in}}{2}. \tag{S7}$$

In Fig. S11*B* we plot the evolution of $i_S$ as a function of time for the experiment characterized by $A_{\rm in} = 100$ mm. We find that the pulse propagates at a constant velocity of 279 loop/s and then slightly accelerates when it approaches the end because of boundary effects - a behavior that is fully consistent with a solitary wave.

Finally, in Fig. S11 we characterize the evolution of the center of mass of the Slinky during the propagation of the pulse. To this end, we calculate the displacement of the center of mass, $u_{\rm CM}$ as

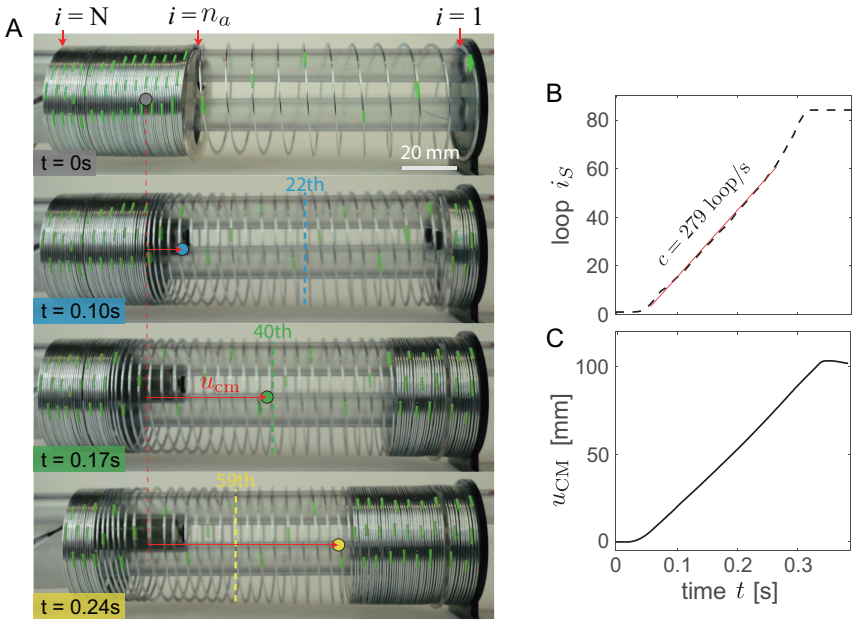


*Figure S11: Propagation of the soliton changes the position of the center of mass. (A) Snapshots of the Slinky during the test at $t = 0$ s, 0.10 s, 0.17 s and 0.24 s. The circular marker represents the position of the center of mass, while the dashed line indicates $i_S$. (B) Evolution of $i_S$ as a function of time. (C) Evolution of the displacement of the center of mass, $u_{CM}$, as a function of time. Photo Credit: Bolei Deng, Harvard University.*

(Fig. S11*A*)

$$u_{\mathrm{CM}}(t) = \frac{1}{N_m}\sum_{i=1}^{N_m}\left[u_i(t) - u_i(t=0)\right] \tag{S8}$$

where $N_m$ denotes the number of markers tracked during the experiment and $u_i(t)$ and $u_i(t=0)$ are the displacement of the $i$-th loop at time $t$ and at time $t = 0$ (i.e. just before the electromagnet is turned off), respectively. In Fig. S11*B* we report the evolution of $u_{\mathrm{CM}}$ as a function of time for the experiment with $A_{\mathrm{in}} = 100$ mm. We find that, as the pulse propagates through the Slinky, the center of mass moves towards the right. This suggest that the propagation of pulses in the Slinky can be harnessed to induce locomotion, since the structure is moved rightward when the pulse reaches its left end (Fig. S8*D*).

## 4 Propagation of non-linear waves: mathematical model

To get more insights into the propagation of non-linear waves in the Slinky, we derive a mathematical model. To this end, we model the Slinky as a one-dimensional array of concentrated masses $m$ connected by nonlinear springs (see Fig. S12). Each spring represents the elastic response of an individual loop (which is described by Eq. (S1)), whereas each concentrated mass represents its mass. The governing equations for such system can be written as,

$$m\frac{\partial^2 u_i}{\partial t^2} = F\left(u_{i+1} - u_i\right) - F\left(u_i - u_{i-1}\right), \tag{S9}$$

where $u_i$ denotes the displacement in longitudinal direction of the $i$-th mass and $F\left(u_{i+1}-u_i\right)$ is the non-linear force of the spring connecting the $(i+1)$th to the $i$th springs. Note that for the Slinky considered in this study $m = 1.01$ g and $F\left(u_{i+1}-u_i\right)$ is given by Eq. (S1).

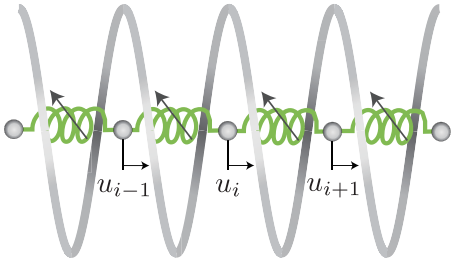


*Figure S12: A schematic of our model. Each non-linear spring represents the elastic response of an individual loop, whereas each concentrated mass represents its mass.*

Next, we introduce the continuous function $u\left(x,\,t\right)$ that interpolates the displacement of the $i$-th mass as,

$$u\left(x=i,\,t\right)=u_i(t), \tag{S10}$$

where $\xi$ denotes the loop number. Moreover, we assume that the width of the propagating waves is much larger than the unit cell size, so that $u_{i+1}$ and $u_{i-1}$ can be expressed using Taylor expansion as

$$u_{i\pm1}(t)=u\left(\xi=i\pm1\,,t\right)\approx u\Big|_{i,\,t}\pm\frac{\partial u}{\partial\xi}\Big|_{i,\,t}+\frac{1}{2}\frac{\partial^2 u}{\partial\xi^2}\Big|_{i,\,t}\pm\frac{1}{6}\frac{\partial^3 u}{\partial\xi^3}\Big|_{i,\,t}+\frac{1}{24}\frac{\partial^4 u}{\partial\xi^4}\Big|_{i,\,t} \tag{S11}$$

Substitution of Eqs. (S10) and (S11) into Eq. (S9) yields the continuum governing equation,

$$\frac{1}{c_0^2}\frac{\partial^2 u}{\partial t^2}=\frac{\partial^2 u}{\partial\xi^2}+\frac{1}{12}\frac{\partial^4 u}{\partial\xi^4}+3\alpha\left(\frac{\partial u}{\partial\xi}\right)^2\frac{\partial^2 u}{\partial\xi^2} \tag{S12}$$

where $c_0=\sqrt{k/m}$ is the velocity of linear waves in the long wavelength regime. Eq. (S12) has been shown to admit analytical solution in the form [Ref. 34 in main text]

$$u=-\sqrt{\frac{2}{3\alpha}}\arctan\left[\tanh\left(\frac{\xi-\xi_0-c\,t}{W}\right)\right]+\frac{\pi}{4}\sqrt{\frac{2}{3\alpha}}, \tag{S13}$$

where $\xi_0$ identifies the position of the solitary wave at $t=0$ and $c$ and $W$ are the speed and the characteristic width of the pulse, respectively. By substituting Eq. (S13) into Eq. (S12), we find that the latter is satisfied only if

$$W=\sqrt{\frac{1}{3\left(c^2/c_0^2-1\right)}}, \tag{S14}$$

which provide the relation between $c$ and $W$. In Fig. S13*A*, we show the evolution of the propagation velocity as function of the width predicted by Eq. (S14).

Moreover, since the solitary wave propagates maintaining its shape, we require the maximum strain in the Slinky (i.e. $\max(\partial u/\partial\xi)$) to be equal to that imposed to the $n_a$ loops before turning off the

electromagnets (i.e. $A_{\text{in}}/n_a$)

$$\frac{A_{\text{in}}}{n_a} = \max\left(\frac{\partial u}{\partial x}\right) = \sqrt{\frac{2}{\alpha}\left(\frac{c^2}{c_0^2} - 1\right)}, \tag{S15}$$

from which we obtain

$$c = c_0\sqrt{1 + \frac{\alpha A_{\text{in}}^2}{2n_a^2}}. \tag{S16}$$

Finally, the amplitude of the soliton can be calculated as

$$A_{\text{s}} = u(\zeta \to \infty) - u(\zeta \to -\infty) = \frac{\pi}{\sqrt{6\alpha}}. \tag{S17}$$

For the Slinky considered in this study (for which $\alpha = 155.1$ m$^{-2}$) we find that $A_{\text{s}} = 103$ mm. Therefore, in excellent agreement with our numerical experimental results, the model reveals that our system supports the propagation of solitary waves only with amplitude $A_{\text{in}} \approx A_{\text{s}} = 103$ mm. Note that the validity of the model is also confirmed by the results presented in Fig. S13B, where we compare the theoretical predictions (lines) with experimental results (markers) and find very good agreement between the two set of data (note that in the analytical solution we use $\xi_0 = 110$).

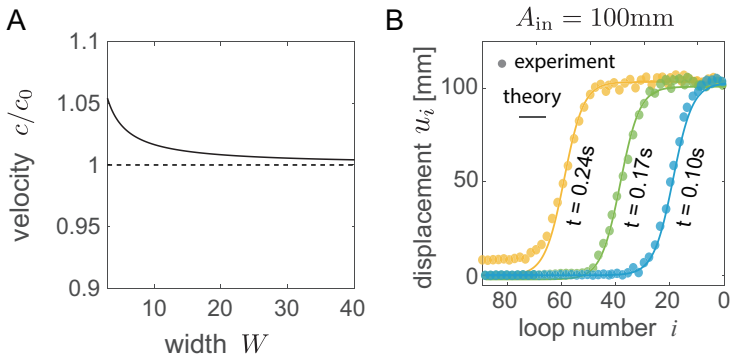


*Figure S13: Theoretical results. (A) Relation between the width $W$ and velocity $c$ as predicted by Eq. (S14). (B) Comparison between analytical solution ( Eq. (S13)) and experimental results obtained for a test characterized by input amplitude $A_{in} = 100$ mm.*

## 5 Description of Supporting Movies

**Movie S1: Effect of the electromagnet field on locomotion ($m_{\text{h}}/m_{\text{tot}}$=0.23, $n_a = 10$ and $A_{\text{in}} = 100$ mm)**

First, we extend the front 10 loops to $A_{\text{in}} = 100$ mm while keeping the electromagnet on. No motion is achieved. Next, we turn off the electromagnet after stretching the front loops to $A_{\text{in}} = 100$ mm. Remarkably, we find that the propagation of the excited pulses results in forward motion.

**Movie S2: Effect of $m_{\text{h}}$ on locomotion ($n_a$=10 and $A_{\text{in}} = 100$ mm)**

The performance of our Slinky-robot is optimal for $m_{\rm h}/m_{\rm tot}$=0.32. For $m_{\rm h}/m_{\rm tot}$=0.48 $u_{\rm h}^{\rm cycle}$ drops as the weight prevents the head to move forward when the pneumatic actuator is extended.

**Movie S3: Effect of $n_a$ on locomotion ($m_{\rm h}/m_{\rm tot}$=0.32 and $A_{\rm in} = 100$ mm)**

For $n_a = 4$ the pulses are too strong and their energy dissipates via collisions between the loops. For $n_a = 30$ the pulses are too weak and barely propagate.

**Movie S4: Propagation of non-linear waves ($n_a = 10$)**

A slinky with 90 loops is lifted from the substrate and supported by a plastic rod to minimize the friction. By pre-stretching 10 loops near the front and turning off the magnetic electromagnet we initiate elastic waves that propagate towards the back. The green markers are used to track the displacement of every other loop.

**Movie S5: Steering ($m_{\rm h}/m_{\rm tot}$=0.23, $n_a = 10$ and $A_{\rm in} = 100$ mm)**

We can make the robot steer by twisting the last loop at the back of the robot by an angle $\alpha$ before initiating the wave.

**Movie S6: Locomotion on a very rough surface ($m_{\rm h}/m_{\rm tot}$=0.32, $n_a = 10$, $A_{\rm in} = 100$ mm and $\mu = 0.68$)**

For larger values of $\mu$, the frictional forces prevent propagation of the pulses and $u_{\rm h}^{\rm cycle}$ drops significantly.